J. Mech. Phys. Solids 188 (2024) 105676

Contents lists available at ScienceDirect

Journal of the Mechanics and Physics of Solids

journal homepage: www.elsevier.com/locate/jmps

Elastic contact between rough surfaces: Bridging the gap between theory and experiment

Hans Terwisscha-Dekker [a,*], Albert M. Brouwer [b], Bart Weber [a,c], Daniel Bonn [a]

[a] Van der Waals-Zeeman Institute, University of Amsterdam, Science Park 904, 1098 XH Amsterdam, Netherlands
[b] Van 't Hoff Institute for Molecular Sciences, University of Amsterdam, Science Park 904, 1098 XH Amsterdam, Netherlands
[c] Advanced Research Center for Nanolithography (ARCNL), Science Park 106, 1098 XG Amsterdam, Netherlands

ARTICLE INFO

Keywords:
Contact mechanics
Surface roughness
Fluorescence microscopy

ABSTRACT

Friction is generated where solids touch, thus quantitative understanding of the microscopic contact area is crucial to predict macroscopic friction. All surfaces are rough, and typically small-scale roughness rather than macroscopic geometry sets the contact area. Rough contact theories have been developed that predict the contact area, using the surface topography and the mechanical properties of the solids as input. However, the validity of these theories remains under debate. Systematic comparison between theory and experiment has been lacking, due to the experimental difficulty to access the contact area, especially at small length scales where idealised assumptions of contact models may not hold. Here, we use a state-of-the-art fluorescence microscopy technique to directly access the contact area of a glass-glass contact with nanometric out-of-plane resolution. We systematically vary the roughness of the contact and carefully measure the surface topography across length scales. Comparison of high-resolution contact experiments to different contact theories enables us to unambigously conclude that only elastic Persson theory quantitatively describes experimental observations.

1. Introduction

Friction forces are ubiquitous yet hard to predict. Much of the complexity of understanding friction comes from uncertainty about the contact area (Vakis et al., 2018; Weber et al., 2018, 2022): all surfaces are rough to some degree and it is the interplay between surface roughness and mechanical properties that determines the contact area. Contact mechanics theories have been developed that predict a linear relation between contact area and normal force for contact between elastic, rough solids (Greenwood and Williamson, 1966; Bush et al., 1975; Persson, 2001). This finding has been used to explain the often-observed proportionality between friction force and normal force (Amontons' law). However, the validity of rough contact mechanics theories remains under debate (Carbone and Bottiglione, 2008; Müser et al., 2017; Yastrebov et al., 2017): the proportionality constant between contact area and normal force differs between theories, and in general, it is questionable whether the assumptions of rough contact theories, such as idealised elasticity and plasticity across all length scales, are met in reality. Hence, a systematic direct comparison between theory and experiment is needed to find out which contact theory most accurately describes reality.

No surface is exactly the same, thus contact mechanics theories use a simplified description of the topography to predict how contact area A develops as a function of normal force F. In absence of roughness, the elastic contact between a sphere of radius R

* Corresponding author.
E-mail address: h.dekker2@uva.nl (H. Terwisscha-Dekker).

https://doi.org/10.1016/j.jmps.2024.105676
Received 28 February 2024; Received in revised form 23 April 2024; Accepted 4 May 2024
Available online 10 May 2024

contacting a flat surface generates a contact area given by the Hertz solution (Hertz, 1881):

$$A = \pi \left(\frac{3R}{4E^*}\right)^{\frac{2}{3}} F^{\frac{2}{3}}, \tag{1}$$

with $\frac{1}{E^*} = \frac{1-{\upsilon_1}^2}{E_1} + \frac{1-{\upsilon_2}^2}{E_2}$ defining the composite elastic modulus E^* of the contacting materials 1 and 2 with Young's modulus E_i and Poisson's ratio ν_i. If, on the contrary, the contacting surfaces are significantly rough, roughness dominates the contact behaviour rather than macroscopic shape, and contact models that consider contact of nominally flat rough surfaces apply better. In the elastic case the contact area increases linearly with normal force (for small normal forces), and roughness enters the equation through the root-mean-square slope of the combined surface topography, $h'_{rms} = \sqrt{|\nabla h^2|}$:

$$A = \frac{\kappa}{E^* h'_{rms}} F. \tag{2}$$

κ is a constant of order unity that depends on the contact model considered, with values ranging from $\sqrt{\frac{8}{\pi}} \approx 1.6$ (Persson scaling theory (Persson, 2001) as applied in this work) to $\sqrt{2\pi} \approx 2.5$ (Greenwood-Williams multi-asperity theory (Greenwood and Williamson, 1966; Bush et al., 1975)). In fact, Persson derived Eq. (2) as an asymptote at small normal force of a more general relation that describes the complete contact evolution from infinitesimal to full contact:

$$A/A_0 = \mathrm{erf}\left(\frac{\sqrt{\pi}}{2} \frac{\kappa F}{A_0 h'_{rms} E^*}\right), \tag{3}$$

with erf the error function and A_0 a reference 'full' contact area. Adaptations of these rough contact theories have been developed to include plasticity (Zhao et al., 2000, 1987; Persson, 2001) and adhesion (Fuller and Tabor, 1975; Persson et al., 2002; Greenwood, 2017; Müser, 2017).

Comparison between theory and experiments has thus far been very limited for two reasons: (i) it is difficult to experimentally access the contact area (Weber et al., 2022), since the contact is buried between the contacting solids and contact structure may extend down to the smallest length scales, and (ii) surface roughness exists across many length scales (Gujrati et al., 2021) and the root-mean-square slope h'_{rms} depends strongly on the smallest length scale over which the topography is measured (Jacobs et al., 2017), which makes the theory prediction dependent on the resolution of the topography measurement instrument. These fundamental challenges have limited the systematic comparison between analytical contact mechanics theories and experimental contact observations to 3D-printed surfaces contacting soft substrates (McGhee et al., 2017; Bennett et al., 2017). In these cases, the surfaces are especially designed to feature no small-scale roughness in order to keep h'_{rms} well-defined, and the soft substrate ensures a large contact area that is relatively easy to observe. In contrast, for materials encountered in real life, the surface topography is not known *a priori* and roughness and roughness-induced contact structure may extend down to nanometer scales, particularly for hard materials. At these small length scales, many of the assumptions of contact mechanics theories, such as linear elasticity and no adhesion, may be violated. Therefore, it remains an open question whether elastic rough contact theories can accurately predict the contact area of experimental, non-idealised contacts at small length scales.

In this work, we address this question through high resolution contact visualisation experiments of hard-hard sphere-on-flat contacts with a systematically varied roughness. We visualise the contact area using a state-of-the art fluorescence microscopy method that makes use of a fluorescent liquid (Petrova et al., 2018; Allain et al., 2016). For optical reasons, the ideal substrate in this type of experiment is a float glass microscopy coverslip; to study a high E^* contact we use a sphere also made of glass as the contacting counter material. In a contact visualisation experiment, the glass-glass contact is immersed in fluorescent liquid, which fills the gap between the two surfaces. As every molecule of this liquid is fluorescent, the measured fluorescence intensity is directly proportional to the local gap, with molecular-scale height resolution. At the points of contact, the liquid is squeezed out between sphere and flat, which allows to measure contact with nanometric out-of-plane resolution. Surface roughness of the contacting materials is characterised using a combination of methods to cover all length scales observable in the contact experiment: optical profilometry for the larger scales (up to 200 μm) and atomic force microscopy (AFM) for the smaller scales (down to 49 nm). Comparison between experimentally measured contact area and theory predictions based on the measured topography shows unambigously that elastic Persson theory (Eq. (3)) can accurately predict experimental contact mechanics without any adjustable parameter, from tiny contact fractions up to full contact.

2. Methods

2.1. Contact experiment

To simultaneously impose a carefully monitored normal force and visualise the contact, we mount a home-built vertical translation stage on top of an inverted confocal microscope (Zeiss Axiovert 200, 63x objective). A glass sphere (Sigmund Lindner, soda-lime glass, $R = 1.84$ mm) is attached to a force sensing beam (Zemic, 5N) that is rigidly connected to the vertical translation stage, which allows us to bring the glass sphere into contact with a microscopy glass coverslip (VWR, borosilicate glass, 22 × 22 × 0.1 mm) while monitoring the normal force. Contact composite elastic modulus E^* is 36 GPa (elastic moduli and Poisson's ratios of materials obtained from manufacturers). The contact is immersed in a droplet of tetrazine-based fluorescent liquid (3,6-bis((2-ethylhexyl)oxy)-1,2,4,5-tetrazine). The fluorescent liquid is excited with 514 nm laser light, the light emitted by the liquid

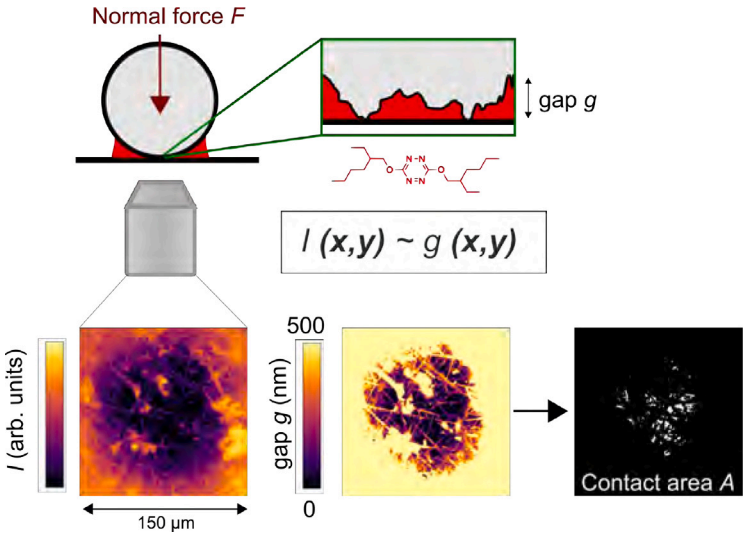

Fig. 1. The contact between a glass sphere and a glass coverslip is immersed in tetrazine-based fluorescent liquid. As this liquid fills the gap between sphere and coverslip, the fluorescent intensity per pixel is directly proportional to the local gap height (for gaps < 500 nm). Separating contact and non-contact pixels by choosing an appropriate threshold, we determine the contact area A at a given normal force F.

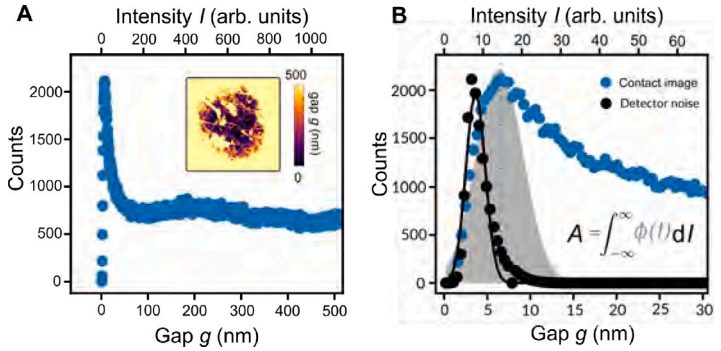

Fig. 2. **A**: The fluorescence intensity (equivalently, local gap) histogram of a contact image (shown as inset) shows a distinct peak close to zero intensity/gap. This peak corresponds to the area of solid–solid contact, where the fluorescent liquid is squeezed out and fluorescence intensity drops to a minimum. **B**: To separate the contact area contribution from the rest of the contact image histogram, we assume a Gaussian intensity distribution in the contact and fit a Gaussian (grey area) to the lower intensity side of the contact peak (left of the blue dotted line). Contact area A is determined by integrating the fitted contact area histogram ϕ. Note that the intensities in the contact area are quite similar to the Gaussian detector noise (black markers, black line is Gaussian fit) measured in absence of excitation light, except for a slight shift and widening due to optical convolution and unresolved contact structure. The detector noise histogram is renormalised to have the same maximum as the contact image histogram.

is recorded through a 560–615 nm bandpass filter. As every molecule of the liquid is fluorescent and reabsorption is negligible, the fluorescence intensity is directly proportional to the local gap between sphere and coverslip (Petrova et al., 2018). By carefully calibrating the relationship between fluorescence intensity and gap height (see Fig. 6 in Appendix), we can measure local gaps of up to a few 100 nm with molecular-scale height resolution. Fig. 1 shows the measured intensity image for a typical contact of a roughened glass sphere pressed on the microscopy coverslip, where intensity scales linearly with local gap. By applying a suitable threshold intensity value that discriminates between areas of contact (low intensity) and areas where the surfaces are separated (higher intensity), we obtain an image of the contact area A.

Determining which parts of the fluorescence image are in contact and which parts are not is not trivial. Ideally, the intensity in the contact area would be zero, since all fluorescent liquid is squeezed out upon solid–solid contact. However, the intensity in the contact always remains non-zero, for multiple reasons: (i) there is detector noise even in the absence of excitation light, (ii) the measured image is a convolution of the 'real' image and the point spread function (PSF) of the imaging system, which means that pixels corresponding to the contact area may receive light from nearby non-contact areas, and (iii) the area covering one pixel may consist of areas of contact and non-contact at smaller scales. Due to these factors, the contact area contributes a sharp but finite width peak at very small intensity to the fluorescence image intensity histogram (Fig. 2A), which we use to determine the contact area A from the fluorescence image.

The combined effects of detector noise, optical convolution and sub-pixel contact structure lead to a Gaussian intensity distribution $\phi(I)$ in the contact area, which is shifted and widened compared to the independently determined Gaussian detector noise (Fig. 2B). We reconstruct $\phi(I)$ from the contact image histogram by fitting a Gaussian to the lower intensity side of the maximum, because for higher intensities, the contact area contribution becomes overwhelmed by contributions from non-contact areas. Integrating the fitted Gaussian curve gives a quantitative estimate of the contact area A. Comparing the mean intensity in the contact area with the mean intensity of detector noise as a reference, we observe a difference in intensity which corresponds to a gap of only 3.3 nm. Thus, the employed fluorescence contact visualisation method is capable of discriminating between contact and non-contact with a height resolution of a few nanometer. It is important to note that in previous work we have shown that thin boundary films of the fluorescent liquid, which partially wets the glass, remain at the solid-on-solid interface, especially for the smoothest interfaces (Petrova et al., 2019). Such films may also play a role in protecting the glass surfaces from the most extreme contact pressures and strains.

Due to overlap between intensity distributions of contact and non-contact areas (Fig. 2B), it is not possible to determine a threshold intensity separating contact and non-contact areas at single pixel level. To get still some qualitative insight into contact morphology, we approximate the contact area image by setting a threshold intensity I_{thr} such that the total contact area of pixels with intensity lower than this threshold $A_{I<I_{thr}}$ is approximately equal to the contact area A determined by the Gaussian fit of the contact peak.

2.2. Sample roughening and roughness characterisation

An initially smooth glass sphere is roughened by shaking the sphere in a container with a piece of silicon carbide sandpaper. Shaking is done for 3 h to create a uniformly rough surface. Different sandpaper grit sizes are used to create samples of different roughness. The roughest sphere that we use in contact experiments is roughened with P600 sandpaper, the smoothest sphere is the as-received sphere.

We use two instruments to characterise the surface roughness across length scales. A laser scanning confocal profilometer (Keyence-VX100, 404 nm laser, 50x magnification) scans the surface topography with a pixel size of 138 nm and a scan size of 212×283 μm. For the smaller length scales, we use an atomic force microscope (Bruker Dimension Icon, tapping mode), scanning across 50×50 μm with 49 nm resolution.

3. Contact morphology

We bring a glass sphere, smooth or roughened to a certain degree, in contact with a glass coverslip in presence of a droplet of fluorescent liquid, to directly see how contact develops as a function of normal force. The contact images shown in Fig. 3 reveal different contact mechanics regimes, depending on roughness. For the roughest sphere, the contact consists of multiple 'island'-like, unconnected areas, while the smoothest sphere exhibits an almost continuous and circular contact, in agreement with the Hertz solution. Intermediate roughness contacts are in between the two extremes: contact patches are larger and more confined to the Hertzian contact circle for increasingly smooth spheres. With increasing normal force, both existing contacts grow and new contacts appear, gradually filling up the Hertzian contact circle. Our findings demonstrate a roughness-induced transition in contact regimes, from roughness-dominated contact islands to geometry-controlled Hertzian contact. Most of the contact patches are confined to the contact circle, which hints at an interplay between microscale roughness and macroscopic spherical geometry.

4. Roughness characterisation across length scales

To make quantitative contact area predictions based on rough contact theories, we need detailed knowledge about the surface topography of the contacts under study. Roughness typically exists across many length scales, and we use two different techniques to capture the surface topography of the glass surfaces: optical profilometry to access the larger length scales, and atomic force microscopy (AFM) to accurately measure small length scales with high lateral and vertical resolution. By combining AFM and optical profilometry, we encompass all the length scales over which contacts are measured in the contact experiment, from the contact image field-of-view (200 μm) down to the contact image pixel size (98 nm).

To obtain a unified statistical description of the surface topography over all the length scales measured, we decompose the real-space surface topography into a spectral representation, using the power spectral density (PSD). After subtracting the macroscopic curvature from the surface topography data, we calculate the radially-averaged PSD C^{iso} as a function of radial wavevector $q = 2\pi/\lambda$ for both AFM and profilometer data using a publicly available code (Jacobs et al., 2017; Röttger et al., 2022) (Fig. 4B). AFM and profilometer C^{iso} partly overlap, however at small length scales the profilometer is less accurate due to the finite size point spread function of the optics involved causing blurring of the heights measured. Indeed optical profilometry is known to sometimes include artefacts caused by optical, rather than roughness, effects; stylus profilometry can be an alternative for measuring roughness at larger length scales. From AFM and profilometer C^{iso} curves, we create a composite C^{iso} that follows profilometer and AFM data at large length scales and AFM data at small length scales (black line in Fig. 4C).

The root-mean-square surface slope $h'_{rms} = \sqrt{|\nabla h^2|}$ is the statistical quantity we want to extract from the surface topography, since it determines the contact area for a given normal force in rough contact theories (Eq. (2)). We determine h'_{rms} by integration over the composite PSD:

$$(h'_{rms})^2 = \frac{1}{2\pi}\int_{q_0}^{q_1} q^3 C^{iso}(q) dq \tag{4}$$

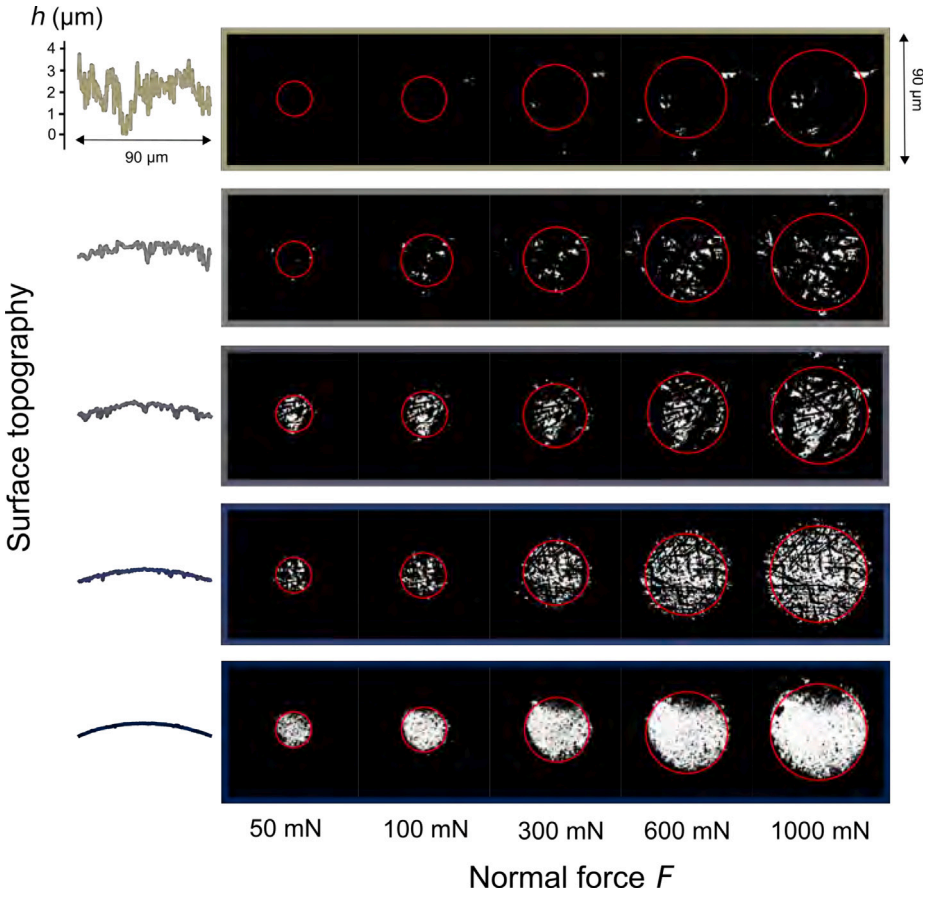

Fig. 3. The measured contact images of glass-on-glass contact of varying roughness show a continuous transition between contact regimes: from roughness-controlled contact islands for rougher spheres to an almost continuous circular Hertz contact for smoother spheres. The corresponding Hertz contact contour is plotted in red. For the roughest sphere, a small fraction of the contact lies outside the shown image. Normal forces for the contact images may vary from the normal forces shown on the x-axis, because the experiment is displacement-controlled rather than normal force-controlled. The plotted Hertz circle always corresponds to the exact normal force of that contact image.

The numerical value of h'_{rms} calculated from Eq. (4) depends on the smallest wavevector q_0 (largest length scale) and largest wavevector q_1 (smallest length scale) considered, especially q_1 has a very strong influence given the q^3 factor in the integrand. As we want to use h'_{rms} to predict contact areas which we compare to contact visualisation data, the integration limits q_0 and q_1 should follow naturally from the length scales observable in the contact visualisation experiment. The largest wavelength that could be resolved in the contact experiment is on the order of the microscopy field of view: $q_0 = q_{FOV} = 2\pi/\lambda_{FOV}$ with $\lambda_{FOV} = 200$ μm. On the other hand, the finest detail that can be resolved with the microscope has a typical size which is determined by the optical point spread function (PSF). The PSF can be approximated as a 2-dimensional Gaussian with a full width at half maximum (FWHM) of 600 nm, which is larger than the theoretical diffraction limit due to imperfections in the imaging method (Hsia et al., 2021). The smallest resolvable feature in the contact experiment has a typical size of 600 nm, which corresponds roughly to a wavelength $\lambda_{PSF} = 2 \cdot 600$ nm in the surface topography PSD. To evaluate h'_{rms} from Eq. (4), the largest wavevector considered will then be $q_1 = 2\pi/\lambda_{PSF}$. The calculated h'_{rms} of the rough spheres used are between 0.01 and 0.4.

5. Quantitative comparison of theory and experiment

The carefully determined surface slope h'_{rms} allows us to make detailed comparison between predictions of elastic rough contact theories and measured contact areas. Fig. 5A shows the measured contact areas as a function of normal force for the spheres with varying roughness, with rougher spheres (lighter colours) showing more deviation from the 'smooth' Hertzian contact (red line). Given that contacts form almost exclusively within the Hertzian contact circle (Fig. 3), we rescale A with A_{Hertz} and F to a reduced pressure $p^* = F/(A_{Hertz} h'_{rms} E^*)$, shown in Fig. 5B. The contact area data for all degrees of roughness form a continuous curve, from tiny contact fractions ($A/A_{Hertz} < 0.01$) up to full Hertzian contact. Multi-asperity and asymptotic Persson theory (Eq. (2), dotted and dashed lines in Fig. 5B) that predict linear increase of A with F (equivalently, linear increase of relative contact area A/A_{Hertz}

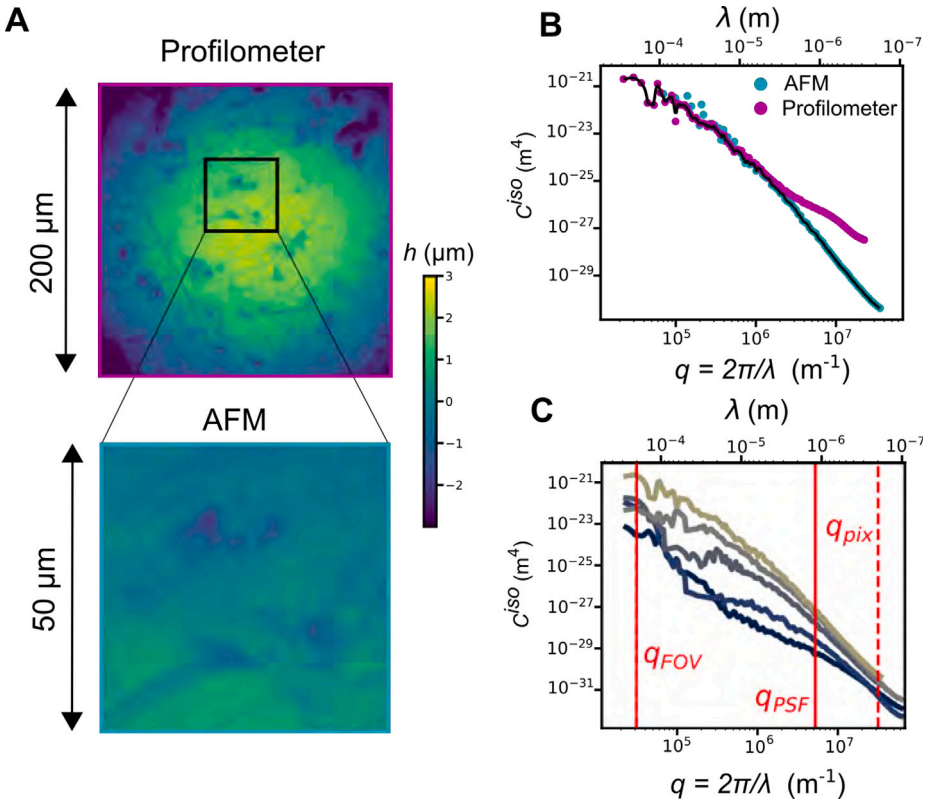

Fig. 4. **A** Optical profilometer and AFM measurements reveal the topography of the roughened glass spheres. The microscopy coverslip used in the contact experiments is effectively flat on the lateral length scales considered (Weber et al., 2019), thus the sphere roughness defines the contact roughness. **B** Power spectral density C^{iso} of AFM and profilometer topographies allow to construct a composite C^{iso} (black line), following the AFM data at small length scales and both AFM and profilometry data at large length scales. **C** Composite power spectral densities C^{iso} of the rough spheres used in the contact experiment (colours of the curves correspond to those used in Fig. 3). Wavevectors corresponding to relevant length scales from the contact visualisation experiment are indicated: microscopy field-of-view (q_{FOV}), point spread function FWHM (q_{PSF}) and pixel size (q_{pix}). Since the PSF rather than the pixel size determines the resolution of the contact visualisation experiment, the surface slope h'_{rms} is calculated by integrating C^{iso} between q_{FOV} and q_{PSF}, thereby excluding the high frequency part of the AFM based spectrum in which measurement noise becomes dominant.

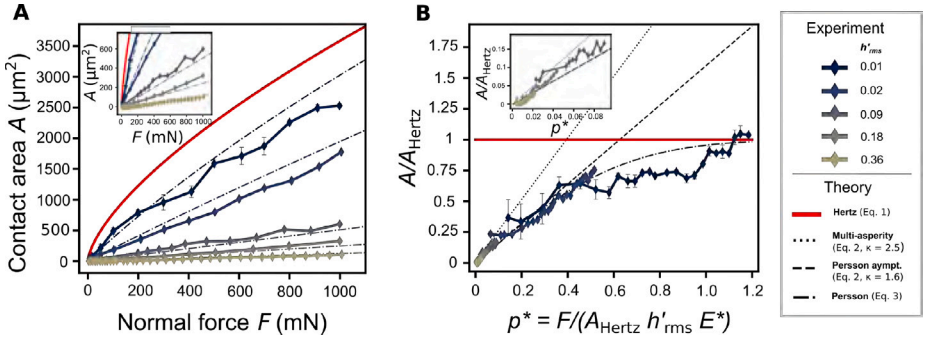

Fig. 5. **A** Contact area A is shown as a function of normal force F for spheres of different roughness. The uncertainty in the measured contact area is quantified through the error margin in the Gaussian fit parameters that are used to analyse the contact image intensity distributions (see Fig. 2). Predictions of Persson theory (Eq. (3)) are shown with dash dotted lines. **B** Rescaled contact area A/A_{Hertz} as a function of reduced pressure p^* for contacts of different roughness reveals a continuous transition from linear increase of A with F (equivalently A/A_{Hertz} with p^*) to Hertzian contact mechanics. Persson theory accurately predicts the contact areas across contact regimes, while multi-asperity and asymptotic Persson theory can only describe the small contact area regime, up to $A/A_{Hertz} \approx 0.2$.

with reduced pressure p^*) can only describe contact area for small contact fractions, up to $A/A_{Hertz} \approx 0.2$. The full contact area evolution is accurately described with the full Persson theory (Eq. (3), dash-dotted line in Fig. 5). Converting back to contact area as a function of normal force, we see that the Persson theory prediction matches well the experimental data over the whole range of roughnesses (Fig. 5A). Thus, we directly experimentally show that, given accurate knowledge about the surface topography at the relevant scales, elastic Persson contact theory correctly predicts the contact area of a rough glass-on-glass over the whole range of contact regimes, without need for any adjustable parameters. Notably, these findings apply to any interface that is governed by linearly elastic deformations, as the theory only relies on the assumption of linear elasticity for the material behaviour.

6. Discussion

In the presented comparison between theory and experimental observation, the concept of *length scales* has been very important. We have experimental access to the contact area across certain lateral length scales, and we determine the surface slope h'_{rms} that sets the theory prediction across the same length scales of the topography. The smallest length scale considered has a huge influence on the value of h'_{rms}, e,g, had we not taken into account the microscopy point spread function and used the pixel size as the smallest length scale to determine h'_{rms} ($q_1 = q_{pix}$ in Fig. 4), then h'_{rms} is two times higher and the predicted contact area two times lower for some measured surface topographies. As for the contact experiment, we have no reason to assume that contact structure does not extend to smaller length scales than the resolution of our microscopy set-up. This raises the question whether the experimentally determined contact area is the *real* contact area that determines its functional properties. When one wants to compute a functional property of a contact, such as the friction coefficient, adhesion strength, or flow permittivity, the physics at play will determine the smallest relevant length scale, such as the length scale over which the topography is flattened by plastic deformation (Weber et al., 2019), length scale of adhesive interaction (Thimons et al., 2021), or the size of a liquid molecule. Thus, there is no well-defined *real* contact area to compare theory predictions against, rather a measured scale-dependent contact area that we compare against a scale-dependent prediction, which allows us to compare contact theories and conclude that Persson theory is consistent with experimental reality. We hypothesize that at the largest experimental loads -where Persson theory slightly overestimates the experimentally observed contact area- trapped pockets of fluorescent liquid may carry part of the applied force. Such sealing effects are predicted theoretically (Lorenz and Persson, 2010) and form an appealing subject for future experiments.

From our presented analysis of glass-glass contact area data, it becomes evident that glass contact mechanics is excellently described with a purely elastic rough contact mechanics theory. In contrast, previous experimental studies have attributed a large role to plasticity in the mechanics of rough, hard contacts, including glass (Dieterich et al., 1996; Ovcharenko et al., 2006). An important reason for the discrepancy between our and previous results is the improved lateral and especially out-of-plane resolution of our contact visualisation method. This high resolution allows us to resolve small features corresponding to elastic deformations, while in lower resolution contact visualisation experiments these features appear larger and more 'smeared out', which has a similar effect as introducing plasticity in a contact theory (Hyun et al., 2004; Pei et al., 2005). To understand why glass behaves elastically in our experiments, it is important to note that the small-scale hardness is much higher than the hardness measured in a macroscopic indentation experiment. For example, for the roughest contact that we measured, the mean contact stress ($\approx$ 10 GPa, see Fig. 5A, inset) is already two times higher than the indentation hardness reported in literature for soda-lime glass ($\approx$ 5 GPa) (Dieterich et al., 1996). Linear elasticity can describe our data over the range of length scales probed here. At even smaller (nanometric) lateral scales plasticity and other non-linear effects may still become important. To go to very small length scales theoretically, one may combine continuum theories such as the one used here with atomistic simulations.

The formulation of Persson theory that we use to describe our results (Eq. (3), with $A_0 = A_{Hertz}$) captures the interplay between macroscopic geometry and microscopic roughness that we observe experimentally: the Hertz circle confines the roughness-controlled contact patches (Fig. 3). Persson theory describes how the nominal (or local) pressure distribution is modified by addition of roughness at different length scales. A special aspect of sphere-on-flat contacts is that the pressure distribution for a smooth spherical contact is parabolic (Hertzian) instead of flat. Müser showed (Müser, 2016) that accounting for the Hertzian pressure distribution leads to relatively mild differences in the predicted contact area, which is in line with our data which are well in agreement with Persson theory even though we do not correct for the Hertzian pressure distribution. Also qualitatively, in Fig. 3, we see little concentration of contact at the centre of the Hertzian contact circle, which would be expected if the parabolic pressure profile of a Hertzian sphere would play a big role. We conclude that the rough contact pressure easily overwhelms the geometrical pressure distribution, and thus the contact effectively behaves as a nominally flat rough contact confined to a disk with radius equal to the Hertz radius.

7. Conclusion

The litmus test of a rough contact mechanics theory is whether it can quantitatively predict the experimentally measured development of contact area with normal force, given the mechanical properties and surface roughness of the contacting materials. In this study, we have performed high-resolution fluorescent liquid contact visualisation experiments of glass-glass sphere-on-flat contacts with a systematically varied roughness. We made a detailed characterisation of the surface topography across length scales, which is used as input for rough contact mechanics theories to predict contact areas that we directly compare to the measured ones. Comparison between theory and experiment unambigously shows that elastic Persson theory accurately predicts the observed contact areas across contact regimes, from tiny contact fractions to full contact. Contact mechanics theories that predict linearity between contact area and normal force (multi-asperity or asymptotic Persson theory) can only describe the contact mechanics for small

contact fractions. The agreement between observation and theory shows not only the validity of Persson theory, it also reveals the somewhat surprising fact that even hard solids at small length scales react predominantly elastically to deformation. These insights suggest that Amontons' law of proportionality between friction and normal force find its origin in elastic contact mechanics between rough surfaces, and predictions from Persson theory such as the normal pressure distribution in a contact may be used to gain microscopic insight into the origins of macroscopic friction. Furthermore, the presented results contribute to the understanding of other interface properties controlled by roughness such as contact stiffness, electrical conductivity, thermal conductivity and the leakage of seals.

CRediT authorship contribution statement

Hans Terwisscha-Dekker: Writing – original draft, Methodology, Investigation, Formal analysis, Data curation, Conceptualization. **Albert M. Brouwer:** Writing – review & editing, Validation, Supervision, Methodology, Conceptualization. **Bart Weber:** Methodology, Formal analysis, Conceptualization. **Daniel Bonn:** Writing – review & editing, Supervision, Project administration, Methodology, Investigation, Funding acquisition, Data curation, Conceptualization.

Declaration of competing interest

The authors declare the following financial interests/personal relationships which may be considered as potential competing interests: Daniel Bonn reports financial support was provided by European Union. If there are other authors, they declare that they have no known competing financial interests or personal relationships that could have appeared to influence the work reported in this paper.

Data availability

Data will be made available on request.

Acknowledgements

We thank prof. Pierre Audebert from ENS Cachan for supplying us with the fluorescent liquid. The Technology Center of the Faculty of Science is acknowledged for skillful technical support. This project has received funding from the European Research Council (ERC) under the European Union's Horizon 2020 research and innovation programme (Grant Agreement No. 833240).

Appendix. Calibration of fluorescence intensity with gap

See Fig. 6

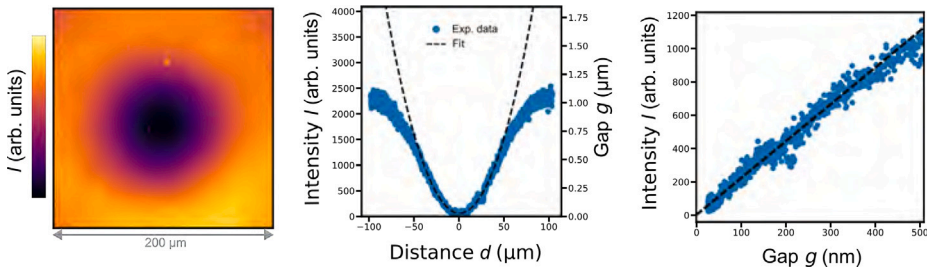

Fig. 6. To calibrate the relationship between fluorescence intensity I and gap g, we put a smooth glass sphere (R = 1.84 mm) on the microscopy coverslip and we immerse the contact in fluorescent liquid. The recorded fluorescence image corresponds to the known gap between a smooth sphere touching a flat surface (left). We fit the spherical profile of the intensity as a function of distance (middle), and obtain a linear relationship between I and g for $g < 500$ nm (right). 1 unit of intensity corresponds to a gap of 0.45 nm.

References

Allain, C., Piard, J., Brosseau, A., Han, M., Paquier, J., Marchandier, T., Lequeux, M., Boissière, C., Audebert, P., 2016. Fluorescent and electroactive low-viscosity tetrazine-based organic liquids. ACS Appl. Mater. Interfaces 8 (31), 19843–19846.

Bennett, A.I., Harris, K.L., Schulze, K.D., Urueña, J.M., McGhee, A.J., Pitenis, A.A., Müser, M.H., Angelini, T.E., Sawyer, W.G., 2017. Contact measurements of randomly rough surfaces. Tribol. Lett. 65 (4).

Bush, A.W., Gibson, R.D., Thomas, T.R., 1975. The elastic contact of a rough surface. Wear 35 (1), 87–111.

Carbone, G., Bottiglione, F., 2008. Asperity contact theories: Do they predict linearity between contact area and load? J. Mech. Phys. Solids 56 (8), 2555–2572.

Dieterich, J.H., Kilgore, B.D., Surcey, U.S.G., Road, M., Park, M., 1996. Imaging surface contacts: power law contact distributions and contact stresses in quartz, calcite, glass and acrylic plastic. Tectonophysics 256, 219–239.

Fuller, K., Tabor, D., 1975. The effect of surface roughness on the adhesion of elastic solids. Proc. R. Soc. Lond. Ser. A Math. Phys. Eng. Sci. 345, 327–342.
Greenwood, J.A., 2017. Reflections on and extensions of the fuller and tabor theory of rough surface adhesion. Tribol. Lett. 65 (4), 1–12.
Greenwood, J.A., Williamson, J., 1966. Contact of nominally flat surfaces. Proc. R. Soc. Lond. Ser. A Math. Phys. Eng. Sci. 295, 300–319.
Gujrati, A., Sanner, A., Khanal, S.R., Moldovan, N., Zeng, H., Pastewka, L., Jacobs, T.D., 2021. Comprehensive topography characterization of polycrystalline diamond coatings. Surf. Topogr.: Metrol. Prop. 9 (1).
Hertz, H., 1881. Über die berührung fester elastischer körper. J. Reine Angew. Math. 92, 156–171.
Hsia, F.C., Franklin, S., Audebert, P., Brouwer, A.M., Bonn, D., Weber, B., 2021. Rougher is more slippery: How adhesive friction decreases with increasing surface roughness due to the suppression of capillary adhesion. Phys. Rev. Res. 3 (4), 1–9.
Hyun, S., Pei, L., Molinari, J.F., Robbins, M.O., 2004. Finite-element analysis of contact between elastic self-affine surfaces. Phys. Rev. E 70 (2), 026117.
Jacobs, T.D., Junge, T., Pastewka, L., 2017. Quantitative characterization of surface topography using spectral analysis. Surf. Topogr.: Metrol. Prop. 5 (1), 013001.
Lorenz, B., Persson, B.N.J., 2010. Time-dependent fluid squeeze-out between solids with rough surfaces. Eur. Phys. J. E 32, 281–290.
McGhee, A.J., Pitenis, A.A., Bennett, A.I., Harris, K.L., Schulze, K.D., Urueña, J.M., Ifju, P.G., Angelini, T.E., Müser, M.H., Sawyer, W.G., 2017. Contact and deformation of randomly rough surfaces with varying root-mean-square gradient. Tribol. Lett. 65 (4), 1–7.
Müser, M.H., 2016. On the contact area of nominally flat hertzian contacts. Tribol. Lett. 64 (1), 1–5.
Müser, M.H., 2017. On the linearity of contact area and reduced pressure. Tribol. Lett. 65 (4), 1–2.
Müser, M.H., Dapp, W.B., Bugnicourt, R., Sainsot, P., Lesaffre, N., Lubrecht, T.A., Persson, B.N., Harris, K., Bennett, A., Schulze, K., Rohde, S., Ifju, P., Sawyer, W.G., Angelini, T., Ashtari Esfahani, H., Kadkhodaei, M., Akbarzadeh, S., Wu, J.J., Vorlaufer, G., Vernes, A., Solhjoo, S., Vakis, A.I., Jackson, R.L., Xu, Y., Streator, J., Rostami, A., Dini, D., Medina, S., Carbone, G., Bottiglione, F., Afferrante, L., Monti, J., Pastewka, L., Robbins, M.O., Greenwood, J.A., 2017. Meeting the contact-mechanics challenge. Tribol. Lett. 65 (4).
Ovcharenko, A., Halperin, G., Etsion, I., Varenberg, M., 2006. A novel test rig for in situ and real time optical measurement of the contact area evolution during pre-sliding of a spherical contact. Tribol. Lett. 23 (1), 55–63.
Pei, L., Hyun, S., Molinari, J.F., Robbins, M.O., 2005. Finite element modeling of elasto-plastic contact between rough surfaces. J. Mech. Phys. Solids 53 (11), 2385–2409.
Persson, B.N., 2001. Elastoplastic contact between randomly rough surfaces. Phys. Rev. Lett. 87 (11), 116101.
Persson, B.N., Bucher, F., Chiaia, B., 2002. Elastic contact between randomly rough surfaces: Comparison of theory with numerical results. Phys. Rev. B 65 (18), 1841061–1841067.
Petrova, D., Weber, B., Allain, C., Audebert, P., Bonn, D., Brouwer, A.M., 2018. Fast 3D microscopy imaging of contacts between surfaces using a fluorescent liquid. ACS Appl. Mater. Interfaces 10 (48), 40973–40977.
Petrova, D., Weber, B., Allain, C., Audebert, P., Venner, C.H., Brouwer, A.M., Bonn, D., 2019. Fluorescence microscopy visualization of the roughness-induced transition between lubrication regimes. Sci. Adv. 5 (12).
Röttger, M.C., Sanner, A., Thimons, L.A., Junge, T., Gujrati, A., 2022. Contact . engineering — Create , analyze and publish digital surface twins from topography measurements across many scales contact . engineering — Create , analyze and publish digital surface twins from topography measurements across many scales. Surf. Topogr.: Metrol. Prop. 10 (3), 035032.
Thimons, L.A., Gujrati, A., Sanner, A., Pastewka, L., Jacobs, T.D., 2021. Hard-material adhesion: Which scales of roughness matter? Exp. Mech. 61 (7), 1109–1120.
Vakis, A.I., Yastrebov, V.A., Scheibert, J., Nicola, L., Dini, D., Minfray, C., Almqvist, A., Paggi, M., Lee, S., Limbert, G., Molinari, J.F., Anciaux, G., Aghababaei, R., Echeverri Restrepo, S., Papangelo, A., Cammarata, A., Nicolini, P., Putignano, C., Carbone, G., Stupkiewicz, S., Lengiewicz, J., Costagliola, G., Bosia, F., Guarino, R., Pugno, N.M., Müser, M.H., Ciavarella, M., 2018. Modeling and simulation in tribology across scales: An overview. Tribol. Int. 125, 169–199.
Weber, B., Scheibert, J., Boer, M.P.D., Dhinojwala, A., 2022. Experimental insights into adhesion and friction between nominally dry rough surfaces. MRS Bull. 47 (December), 1–10.
Weber, B., Suhina, T., Brouwer, A.M., Bonn, D., 2019. Frictional weakening of slip interfaces. Sci. Adv. 5 (4), 1–8.
Weber, B., Suhina, T., Junge, T., Pastewka, L., Brouwer, A.M., Bonn, D., 2018. Molecular probes reveal deviations from Amontons' law in multi-asperity frictional contacts. Nature Commun. 9 (1), 1–7.
Yastrebov, V.A., Anciaux, G., Molinari, J.F., 2017. The role of the roughness spectral breadth in elastic contact of rough surfaces. J. Mech. Phys. Solids 107, 469–493.
Zhao, Y., Lu, Y., Jiang, J., 1987. New elastic-plastic model for the contact of rough surfaces. J. Tribol. 43 (3), 95–101.
Zhao, Y., Maietta, D.M., Chang, L., 2000. An asperity microcontact model incorporating the transition from elastic deformation to fully plastic flow. J. Tribol. 122 (1), 86–93.